# Synthesis of iron-doped TiO$_2$ nanoparticles by ball-milling process: the influence of process parameters on the structural, optical, magnetic, and photocatalytic properties

J. O. Carneiro · S. Azevedo · F. Fernandes ·
E. Freitas · M. Pereira · C. J. Tavares ·
S. Lanceros-Méndez · V. Teixeira

**Abstract** Titanium dioxide (TiO$_2$) absorbs only a small fraction of incoming sunlight in the visible region thus limiting its photocatalytic efficiency and concomitant photocatalytic ability. The large-scale application of TiO$_2$ nanoparticles has been limited due to the need of using an ultraviolet excitation source to achieve high photocatalytic activity. The inclusion of foreign chemical elements in the TiO$_2$ lattice can tune its band gap resulting in an absorption edge red-shifted to lower energies enhancing the photocatalytic performance in the visible region of the electromagnetic spectrum. In this research work, TiO$_2$ nanoparticles were doped with iron powder in a planetary ball-milling system using stainless steel balls. The correlation between milling rotation speeds with structural and morphologic characteristics, optical and magnetic properties, and photocatalytic abilities of bare and Fe-doped TiO$_2$ powders was studied and discussed.

J. O. Carneiro (✉) · S. Azevedo · F. Fernandes · M. Pereira · C. J. Tavares · S. Lanceros-Méndez · V. Teixeira
Center/Department of Physics, University of Minho, Campus of Azurém, 4800-058 Guimarães, Portugal
e-mail: carneiro@fisica.uminho.pt

S. Azevedo
e-mail: csofiaazevedo@fisica.uminho.pt

F. Fernandes
e-mail: b6073@fisica.uminho.pt

M. Pereira
e-mail: mpereira@fisica.uminho.pt

C. J. Tavares
e-mail: ctavares@fisica.uminho.pt

S. Lanceros-Méndez
e-mail: lanceros@fisica.uminho.pt

V. Teixeira
e-mail: vasco@fisica.uminho.pt

E. Freitas
Civil Engineering Department, University of Minho, Azurém Campus, 4800-058 Guimarães, Portugal
e-mail: efreitas@civil.uminho.pt

## Introduction

Textile industry produces a large amount of dyed wastewater. The non-biodegradable nature of the spent dye baths constitutes serious environmental problems [1]. The most emergent technology that is available for the removal of dyes (especially cationic dyes) from textile effluents is the destructive oxidation treatment performed via a photodegradation process induced by dissimilar semiconductor materials. Actually, in recent years there has been a growing interest of the scientific/industrial community in the use of several semiconductor materials in order to act as photocatalysts to initiate photocatalytic reactions on their surfaces [2]. Among the different semiconductor materials, titanium dioxide (TiO$_2$) has been considered the most suitable photocatalyst candidate due to some unique characteristics such as its optical and electronic properties, chemical stability, availability, low cost, and non-toxicity [3]. However, from the point of view of the TiO$_2$ large-scale and practical applications, there seems to be some limitations regarding its election as favorite photocatalyst for the photocatalytic process. Some reasons can be pointed out; one of them is due to its low photo-quantum efficiency that results from the fast recombination of photo-generated electron/hole pairs; the other is the need of using an ultraviolet excitation source to achieve a high photocatalytic activity. In fact, it is well known that TiO$_2$ presents a large band gap ($E_g$, anatase phase $\cong 3.2$ eV and rutile $\cong 3.0$ eV), and it can only make use 3–5 % of the solar

spectrum that reach earth [2]. In this sense, it is important that the production of the $TiO_2$ semiconductor material, sensitive to visible light excitation (using solar energy as the light source), and the reduction of the recombination of photo-generated electron/hole pairs [4] should represent the two characteristics that must be attained to extend $TiO_2$ photocatalytic activity over the electromagnetic spectrum (a condition that is particularly important for outdoor applications).

Extensive research has been carried out to prepare $TiO_2$ photocatalyst that presents these characteristics. For this purpose, many strategies including the doping of $TiO_2$ with transition metals [5–7], noble metal deposition [8, 9], dye sensitized [10], doping of $TiO_2$ with non-metallic or anionic species [11–13] have been investigated. Particularly, doping of $TiO_2$ with transition metal ions was reported [14, 15] as being a good strategy to improve photocatalytic properties and for the enhancement of its visible light response. Specially, Fe-doped $TiO_2$ [16] has been shown to increase the photocatalytic efficiency in many cases. Nevertheless, most of the current methods of synthesizing iron-doped $TiO_2$ nanoparticles face some issues like low production yield and use of some toxic chemical compounds. Therefore, the development of a new fabrication method is still required.

Herein, it is reported the successful synthesis of Fe-doped $TiO_2$ nanoparticles through a simple and efficient mechanical milling technique [17, 18]. Mechanical milling has proved to be an effective and simple method, to produce nanocrystalline powders offering the possibility to obtain large amounts of materials. In a ball-milling process, powders are plastically deformed due to the high-energy impact between balls and the wall of the vial. The result is the rise of the local temperature and pressure (up to several GPa) at the collisions sites of the powder and the balls [19], and in some cases the production of fresh surfaces by fracture of material particles. Meanwhile, the properties of nanopowders obtained by the ball-milling method are affected by different parameters such as the milling-time, ball-to-powder mass ratio, balls diameters, etc.

In this paper, we report that ball milling can be used as a powerful low-cost and "green" method to produce Fe-doped $TiO_2$ nanoparticles, which can be applied as an efficient photocatalyst for large-scale photocatalytic oxidation of dye pollutants present in the effluents of textile industries. The structure, morphologic, optical, magnetic, and photocatalytic properties of bare and Fe-doped $TiO_2$ powders, produced by high-energy ball milling, were investigated using X-ray diffraction (XRD), scanning electron microscopy (SEM), energy dispersive X-ray spectroscopy (EDX), ultraviolet–visible spectroscopy (UV–Vis) diffuse reflectance spectra (DRS), and a vibrating-sample magnetometer (VSM). Given that most recent

**Table 1** Ball milling test conditions

| Sample | Doping ratio Fe in $TiO_2$ (wt%) | Rotation speed (rpm) |
|---|---|---|
| Bare $TiO_2$ | 0 | 0 |
| Undoped $TiO_2$ | 0 | 250 |
| | 0 | 300 |
| | 0 | 350 |
| Fe-doped $TiO_2$ | 10 | 250 |
| | 10 | 300 |
| | 10 | 350 |

research works have studied the influence of milling-time and ball-to-powder mass ratio, the main objective of this article was to study, in detail, the influence and the correlation between milling rotation speeds with structural and morphologic characteristics, optical and magnetic properties as well as the photocatalytic abilities of bare and Fe-doped $TiO_2$ powders were studied and discussed.

## Materials and methods

$TiO_2$ nanoparticles (Aeroxide $TiO_2$ P25) and fine iron powder (purity $\geq 97$ %, particle size of about 40 μm) were obtained from Quimidroga (Spain) and from Sigma-Aldrich® (Portugal), respectively, and used as the starting materials.

### Preparation of samples

Iron-doped $TiO_2$ nanoparticles were prepared by ball milling of $TiO_2$ powders (nanometer size) in a high-energy Planetary Ball Mill PM 400/2 (RETSCH, Germany) in the presence of fine Fe powder.

Milling was done at room temperature in a polytetra-fluoroethylene (PTFE) vial (volume about 35 cm³) using ten hardened steel balls with 10 mm of diameter, keeping powder sample to ball mass ratio at about 1:8 throughout the experiment. The milling process lasted for 5 h with a rotation speed varying from 250 to 350 rpm. The overall ball-milling test conditions are summarized in Table 1.

### Characterization of samples

The XRD was employed to investigate the crystal structure and crystallite size of as-ball-milled powders. The XRD patterns of all samples (including an additional $TiO_2$ sample, which was not submitted to the ball-milling process) were acquired in the range of 20°–90° (2θ) using a Bruker D8 Discover X-ray diffractometer with the conventional Bragg–Brentano geometry. The crystallite sizes

of the photo-catalysts were estimated by applying the Debye–Scherrer equation [19]. The lattice parameters were determined using the following equation:

$$\frac{1}{d_{(hkl)}^2} = \frac{h^2 + k^2}{a^2} + \frac{l^2}{c^2}. \tag{1}$$

Here, $h$, $k$, $l$ are the Miller indices and $a$ and $c$ are the lattice parameters (for a tetragonal phase it is well known that $a = b \neq c$). The value of the lattice spacing $d_{(hkl)}$ for an XRD peak can be determined from Bragg's law:

$$d_{(hkl)} = \frac{\lambda}{2 \sin \theta}. \tag{2}$$

The fraction of anatase phase in $TiO_2$ powders can be estimated from the XRD peak intensities by the following equation [20]:

$$X_A(\%) = \frac{100}{[1 + 1.26(I_R/I_A)]}, \tag{3}$$

where $X_A$ is the weight fraction of anatase phase in the samples, and $I_A$ and $I_R$ correspond to the intensity of the XRD most intense peaks of anatase and rutile, respectively.

The morphology of as-ball-milled powders was examined by scanning electron microscopy (SEM, NanoSEM-FEI Nova 200). The elemental composition of the ball-milled powders was analyzed by EDX with SEM instrument (SEM–EDS).

UV–Vis diffuse reflection spectra (DRS) were obtained for the dry-pressed disk samples ($\varnothing$ 10 mm and pressed at 16 MPa) using a spectrophotometer ScanSpecUV-Vis, ScanSci equipped with an integrating sphere assembly, using Barium Sulfate ($BaSO_4$) as the reference sample. The spectra were recorded at room temperature in air within the range of 300–700 nm. The acquired diffuse reflectance spectra were converted to absorbance through the standard Kubelka–Munk function, $F(R)$. The band-gap energy ($E_g$) of all ball-milled powders was determined using a modified version of the Tauc relational expression [21]. In the modified Tauc's equation, the material absorption coefficient ($\alpha$) can be replaced by $F(R)$, since they are proportional to each other.

The influence of ball-milling rotation speeds in the electrokinetic behavior of the undoped and Fe-doped $TiO_2$ particles was performed by measuring the zeta-potential, $\zeta$ (on a Zetasizer NS 2007 from Malvern Instruments, UK) of the corresponding aqueous dispersions. pH is the most important factor that affects $\zeta$-potential of $TiO_2$ nanoparticles aqueous solutions [22–24]. Zeta-potential measurements and the determination of the isoelectric point (IEP) of the ball-milled $TiO_2$ nanoparticles was performed using a diluted water suspension ($\sim$1 g/L), which was titrated with sodium hydroxide solution (0.5 M); the titration was

done starting at an acidic pH value ($\sim$2) and raised to $\sim$10.

Magnetic measurements were performed at room temperature using a VSM (ADE Technologies).

## Photocatalytic measurements

The photocatalytic activity of all ball-milled powders was evaluated by measuring the degradation rates of Rhodamine B (Rh-B) aqueous (5 mg/L) under ultraviolet (UV) light irradiation. Rh-B (an important xanthene cationic dye) was selected because of its well-defined optical absorption characteristic and good resistance to light degradation (the so-called dye sensitisation). Moreover, this organic dye is one of the most common pollutants present in the effluents from textile industries in developed countries. The photocatalytic experiments of all ball-milled $TiO_2$-based powders were performed in the obtained pressed disk samples.

In a typical experiment, the $TiO_2$-based pressed disk samples were dipped into a flask filled with 100 mL of Rh-B aqueous solution. The system was stirred for 30 min in the dark to reach the adsorption–desorption equilibrium and then placed in a UV simulation chamber. Next, the samples were irradiated with two 15 W UV lamps (F15T8/BLB Duke Essen Germany GE lighting) placed at a distance of about 20 cm above the sample's surface. The average irradiance was around 4 W/m$^2$ (measured with a UV light Meter LTLutron YK-35UV). The absorbance of the Rh-B was monitored during 120 min (at time intervals of 20 min) using a spectrophotometer (ScanSpecUV-Vis, ScanSci) in the range of 300–700 nm. For this, some aliquots of Rh-B solution (3.5 mL) were taken out and then analyzed by monitoring the intensity variation of its main absorption peak (around 564 nm). The same procedure was performed for the bare $TiO_2$ powder (the reference sample). The rate of Rh-B consumed in a chemical reaction can be written as

$$-\frac{dC}{dt} = kC^n \tag{4}$$

where $C$ is the concentration of the Rh-B aqueous solution, $n$ is the kinetic order of the chemical reaction, and $k$ is the rate constant of the photodegradation process.

At low concentrations and for a specific time instant, the absorbance of the solution, $A_t$, is related to its solution's concentration through the Beer–Lambert law, that is, $A_t = \varepsilon l C_t$, where $\varepsilon$ is the molar extinction coefficient, $l$ is the light path length, and $C_t$ is the solution concentration. For a reaction that follows a first-order kinetics, the photodegradation efficiency, $\eta$, of Rh-B can be calculated according to the following equation [25]:
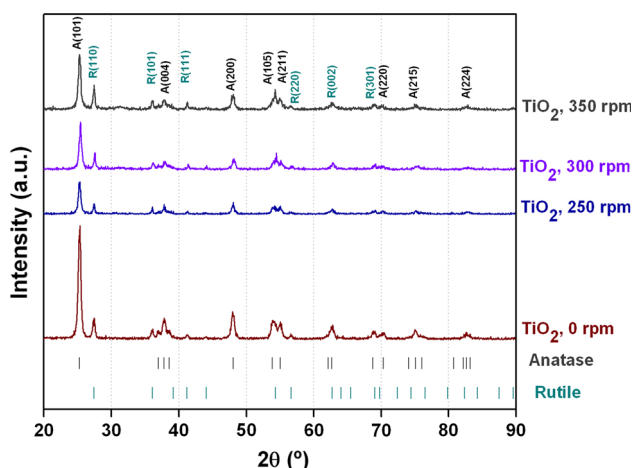
**Fig. 1** XRD patterns of pure undoped $TiO_2$ nanoparticles subjected to different ball-milling rotation speeds (0, 250, and 350 rpm)

$$\eta(\%) = \left[1 - \left(\frac{A_t}{A_0}\right)\right] \times 100 \qquad (5)$$

where $A_0$ is the absorbance at zero time. Therefore, the change of Rh-B concentration can be evaluated by measuring the change in the intensity of its main absorption peak.

## Results and discussion

### XRD analysis

XRD patterns were used to study the effect of ball-milling rotation speed on the phase structure and the phase composition of pure undoped $TiO_2$ and Fe-doped $TiO_2$ nanoparticles (with 10 wt% Fe), milled for 5 h. Figure 1 displays the XRD patterns of pure undoped $TiO_2$ nanoparticles subjected at different ball-milling rotation speeds (0–350 rpm). For these samples, the existence of both anatase and rutile phases can be identified by JCPDS file no. 21–1272 and no. 21–1276, respectively.

It can be seen that in general, with increasing rotation speed, the diffraction peaks become slightly broader and its relative intensities decrease. This effect reveals the material behavior after milling, which should be attributed to the presence of particles with smaller sizes and the formation of lattice defects induced by the milling's mechanical deformation.

For the anatase crystal system, the average crystallite sizes, lattice parameters, and content ratio of anatase phase were determined using the XRD peaks of the crystal planes (101) and (200), whilst for the rutile phase the diffraction planes (110) and (101) were the selected ones. The results of average crystallite sizes, lattice parameters, and weight fraction of anatase phase of undoped $TiO_2$ nanoparticles, as a function of ball-milling rotation speeds, are presented in Table 2.

As summarized in Table 2, for anatase crystalline phase, there is no significant difference between the crystallite size of un-milled $TiO_2$ nanoparticles and that of ball-milled ones. However, for rutile crystalline phase, the corresponding average crystallite sizes present a decrease as the ball-milling rotation speed increases. This behavior can be attributed to the ball's mechanical action, which promotes powder's deformation and induce the creation of more defects during the rising of the rotation speed. In fact, this mechanical-induced distortion is also evidenced by the change in unit cell volume as reported in Table 3. Moreover, it was also found that for the undoped $TiO_2$ nanoparticles the fraction of anatase phase decreases as the rotation speed increases, which indicates an anatase-to-rutile transformation (ART). Actually, higher milling rotation speeds also mean more collisions between the balls and the $TiO_2$ powders; thus, it is expected an increase of the local pressure and temperature at the collisions sites between the balls and the $TiO_2$ powders, which may induce some ART transformation [26].

The effect of Fe-doping on the crystalline structure of the ball-milled $TiO_2$ nanoparticles is shown in Fig. 2, which depicts the XRD pattern of Fe-doped $TiO_2$ powders (10 wt% Fe) at different milling rotation speeds.

For each one of the ball-milling rotation speeds, there are no significant differences between the XRD pattern of Fe-doped and that of undoped $TiO_2$ nanoparticles. In fact, for a particular rotation speed, the fraction of anatase phase in Fe-doped $TiO_2$ nanoparticles has the same magnitude of the undoped ones. This indicates that, when comparing with the ball-milling effect, Fe-doping has no significant influence in ART. Moreover, a Fe-containing phase, (110) was detected in the XRD patterns of Fe-doped $TiO_2$ nanoparticles that suggests the production of some kind of iron segregation in Fe-doped $TiO_2$ nanoparticles, which can be attributed to the high iron content in these samples. On the other hand, the angular position of some XRD peaks was slightly shifted upon doping $TiO_2$ with iron, indicating a small distortion of $TiO_2$ crystal lattice by the iron dopant. Some research works mention that $TiO_2$ lattice distortion can be attributed to the substitution of titanium ion with iron ion because of comparable radii of $Fe^{3+}$ (0.64 Å) and $Ti^{4+}$ (0.68 Å) [27]. For each one of rotation speeds, the substitution of iron in the matrix of $TiO_2$ ($Fe^{3+}$ may occupy some of the $Ti^{4+}$ sites) is supported by some changes in both unit cell volume and crystallite size, as reported in Table 3.

### Electrokinetic behavior of $TiO_2$ powders

Figure 3 compares the $\zeta$-potential curves of the undoped $TiO_2$ samples produced with three different ball-milling

**Table 2** Influence of different ball-milling rotation speeds on the average crystallite size, lattice parameters, and fraction of anatase phase for pure undoped $TiO_2$ nanoparticles

| Rotation speed (rpm) | Crystallite size[a] (nm) | | Lattice parameters[b] (Å) | | | | $X_A$ (%)[c] |
|---|---|---|---|---|---|---|---|
| | Anatase | Rutile | Anatase | | Rutile | | |
| | | | $a$ | $c$ | $a$ | $c$ | |
| 0 | 14.94 | 32.69 | 3.7869 | 9.5360 | 4.5966 | 2.9602 | 82.42 |
| 250 | 14.81 | 30.47 | 3.7858 | 9.5512 | 4.5958 | 2.9589 | 75.16 |
| 300 | 14.76 | 29.67 | 3.7769 | 9.3623 | 4.5774 | 2.9503 | 74.42 |
| 350 | 14.73 | 29.46 | 3.7856 | 9.5501 | 4.5950 | 2.9593 | 66.23 |

[a] Calculated from Debye–Scherrer equation (1)

[b] Calculated from Eq. (1)

[c] Calculated from Eq. (3)

**Table 3** Average crystallite sizes and unit cell volumes obtained at different ball-milling rotation speeds; comparison between undoped and Fe-doped $TiO_2$ samples
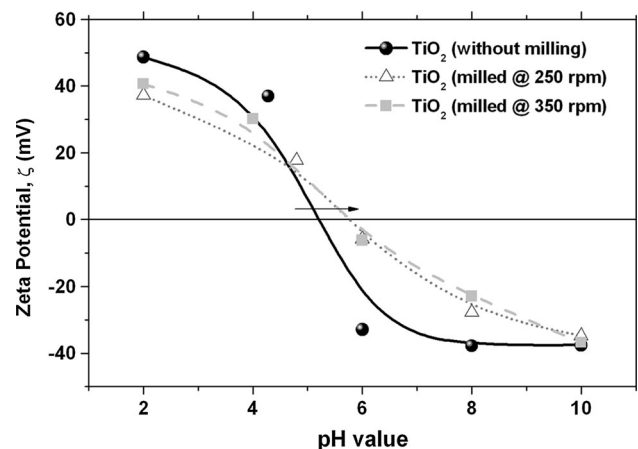
| Rotation speed (rpm) | Undoped $TiO_2$ | | | | Fe-doped $TiO_2$ (10 wt% Fe) | | | |
|---|---|---|---|---|---|---|---|---|
| | Crystallite size[a] (nm) | | Unit cell volume (Å[3]) | | Crystallite size[a] (nm) | | Unit cell volume (Å[3]) | |
| | Anatase | Rutile | Anatase | Rutile | Anatase | Rutile | Anatase | Rutile |
| 0 | 14.94 | 32.69 | 136.75 | 62.55 | – | – | – | – |
| 250 | 14.81 | 30.47 | 136.89 | 62.50 | 15.85 | 25.52 | 135.24 | 62.11 |
| 300 | 14.76 | 29.67 | 133.55 | 61.82 | 15.02 | 23.76 | 134.61 | 61.97 |
| 350 | 14.73 | 29.46 | 136.86 | 62.48 | 14.87 | 22.80 | 134.68 | 62.03 |

[a] Calculated from Debye–Scherrer equation (1)
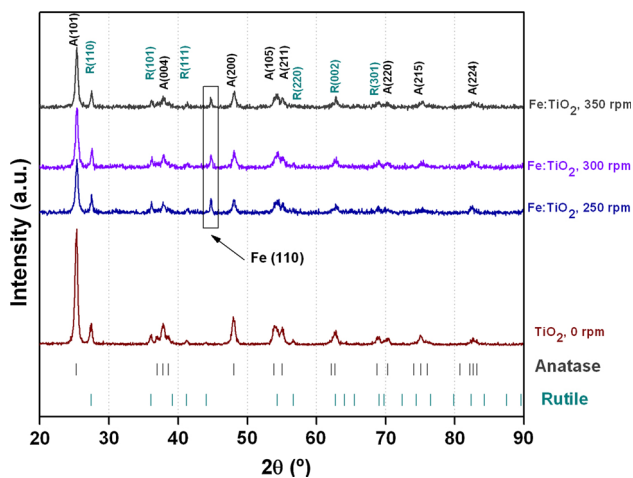


**Fig. 2** XRD patterns of Fe-doped $TiO_2$ nanoparticles subjected to different ball-milling rotation speeds (0, 250, and 350 rpm)



**Fig. 3** Zeta-potential curves versus pH for the undoped $TiO_2$ powders subjected to different ball-milling rotation speeds (0, 250, and 350 rpm)

rotation speeds, that is, maximum (350 rpm), minimum (250 rpm), and zero.

The $\zeta$-potential curve for the non-milled $TiO_2$ sample is typical of unmodified $TiO_2$ nanoparticles as reported by other authors [28]. Anatase and rutile have identical chemical composition but different crystal systems and

thus, their IEP occurs at different pH values, 4.7 versus 6.2 [24]. For the non-milled $TiO_2$ sample, the isoelectric pH value was found to be ~pH 5.2. This is an acceptable value since it reflects the effect of the mixture of two crystalline phases. However, after being subjected to different ball-milling rotation speeds, this sample has

**Table 4** Influence of ball-milling rotation speeds in the IEPs and zeta-potentials of undoped and Fe-doped TiO$_2$ samples

| Rotation speed (rpm) | Undoped TiO$_2$ | | Fe-doped TiO$_2$ |
| --- | --- | --- | --- |
| | Isoelectric pH values (IEP) | Zeta-potential (mV) at IEP | Zeta-potential (mV) at IEP of un-doped TiO$_2$ |
| 0 | 5.200 | 0.0 | – |
| 250 | 5.763 | 0.0 | 19.567 |
| 300 | 5.771 | 0.0 | 4.017 |
| 350 | 5.786 | 0.0 | 1.820 |

experienced some variations on its IEP value (see Fig. 3). This behavior is related with the milling-induced phase transformation as reported in Table 2, that is, for increasing rotation speeds, more anatase transforms into rutile phase and, therefore, causing a change in the IEP value.

Table 4 lists the IEP of the undoped TiO$_2$ powders subjected to different ball-milling rotation speeds, namely (0–350 rpm). For these isoelectric pH values, the $\zeta$-potentials are zero, that is, the electric net charge of the particles is globally null. Table 4 also reports the measured values of $\zeta$-potentials for the 10 wt% Fe-doped TiO$_2$ powders formed at different ball-milling rotation speeds, namely 250, 300, and 350 rpm. For each of ball-milling condition (i.e., for each of rotation speed), the corresponding $\zeta$-potential for Fe-doped TiO$_2$ powders was measured at a pH value equal to the IEP of the undoped TiO$_2$ nanoparticles. In these conditions, it is expectable that, if for some reason the $\zeta$-potential values take any shifts then some kind of chemical modification on particle's surface should be occurring.

Table 4 shows that the $\zeta$-potential values of Fe-doped TiO$_2$ samples are clearly modified (showing non-zero values) relative to that of undoped TiO$_2$ powders, possibly indicating that Fe$^{3+}$ ions can replace Ti$^{4+}$ in the TiO$_2$

lattice and/or promoting some kind of surface chemical modifications.

The solution at pH around to 5.7 makes the surface of the Fe-doped TiO$_2$ powders positively charged, resulting in positive $\zeta$ values. The change of $\zeta$ values suggests that the IEP of Fe-doped TiO$_2$ powders is changing with the increase of ball-milling rotation speeds. It is generally accepted that in aqueous suspensions, TiO$_2$ surfaces are highly hydroxylated [2] resulting in titanol groups, Ti–OH, present at the surface. Surface titanol groups, Ti–OH, are amphoteric and their ionization equilibrium can be written as [29]

$$Ti-OH_2^+ \leftrightarrow Ti-OH + H^+, \tag{6}$$

$$Ti-OH \leftrightarrow Ti-O^- + H^+. \tag{7}$$
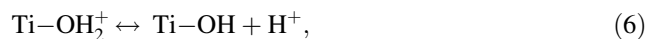
At pH lower than IEP partial protonation of Ti–OH confers to the particles a positive surface charge (Ti–OH$_2^+$ sites) and at pH higher than IEP partial deprotonation of Ti–OH leads to negative Ti–O$^-$ sites [29]. Therefore, Eqs. (6) and (7) suggest that the solution pH also possesses a strong influence on the surface catalytic reactions of TiO$_2$ particles in aqueous medium. The charge on particles, when the pH of the medium is far from the IEP, promotes adsorption phenomena if molecules and ions possess opposite electric charges than the solid surface but inhibits adsorption if adsorbates are characterized by the same type of charge as the solid. An important example is provided by Chen et al. [28], which consider the different adsorption modes of Rhodamine B. At pH below the TiO$_2$ IEP (i.e., positive TiO$_2$ surface, Fig. 3), the dye molecule is adsorbed through the negatively charged carboxylic group, according to Fig. 4. However, for pH higher than the IEP, the TiO$_2$ surface becomes negative and the RhB is adsorbed through the positive charge delocalised across the aromatic ring structure in between the two amino groups (Fig. 5).

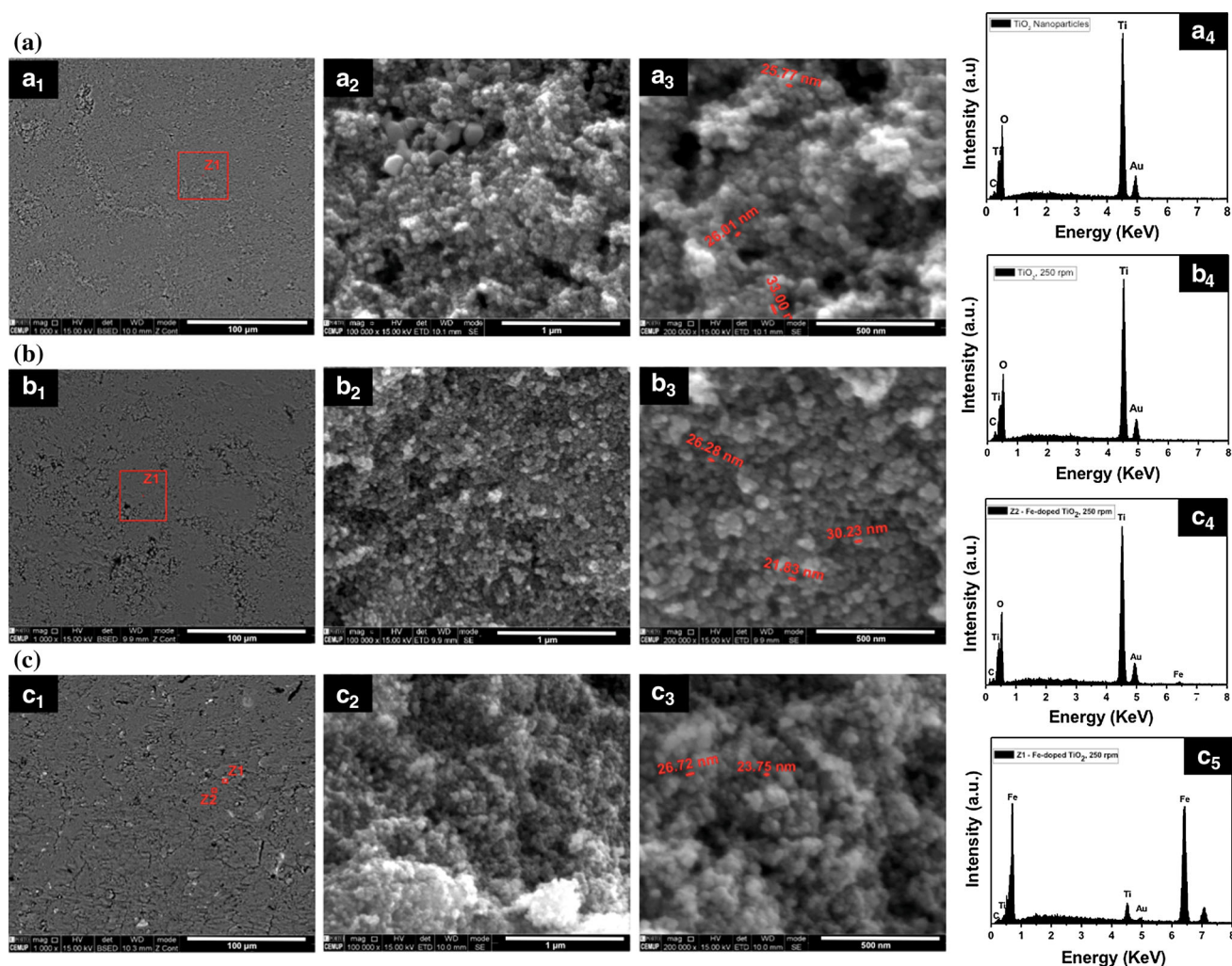**Fig. 4** Adsorption modes of Rhodamine B on charged TiO$_2$ surfaces
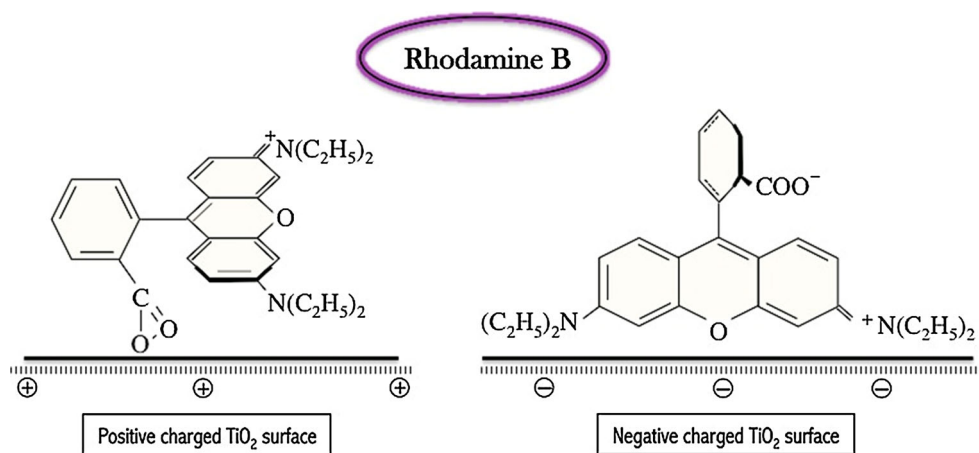
**Fig. 5** SEM micrographs at different magnifications and EDX analysis of **a** undoped TiO$_2$/without milling, **b** undoped TiO$_2$ milled @ 250 rpm, and **c** Fe-doped TiO$_2$/milled @ 250 rpm

Morphology characterization

The surface morphology of TiO$_2$ and Fe-doped TiO$_2$ nanoparticles milled during 5 h with 250 rpm rotation speed is shown in the SEM micrographs in Fig. 5. For comparison purposes, the SEM micrographs of the TiO$_2$ nanoparticles are also presented, which were not subject to the ball-milling process.

SEM analysis shows that, in all the samples, the nanoparticles are irregular in shape, randomly organized, and tend to form agglomerates. Moreover, accordingly with the EDX results presented in Fig. 5 (C4 and C5) iron seems to be dispersed on the surface of TiO$_2$ nanoparticles or between the interfaces of the TiO$_2$ agglomerates. In addition, the surface morphology, nanoparticle's shape and size (between 25 and 30 nm) did not significantly change after ball milling or iron doping. Similar results have also been obtained from XRD (Figs. 1, 2). Nonetheless, the undoped

TiO$_2$ nanoparticles milled at 250 rpm and Fe-doped TiO$_2$/milled at 250 rpm appear to be more agglomerated and more closely packed. By further observing the morphology of the samples, it is possible to notice that the milled TiO$_2$ nanoparticles are rougher which may enhance the absorption of the dyes due to its higher surface area [30]. The EDX analysis reveals the presence of Ti and O for both the undoped TiO$_2$/without milling and undoped TiO$_2$ milled at 250 rpm samples and the presence of Ti, O, and Fe for the Fe-doped TiO$_2$/milled at 250 rpm sample.

UV–Vis diffuse reflectance spectra and band-gap energy

Light absorption measurements were undertaken to derive band-gap information on pure TiO$_2$ and Fe-doped TiO$_2$ powders and have been carried out using UV–Vis diffuse reflectance spectroscopy. This analytical technique is very
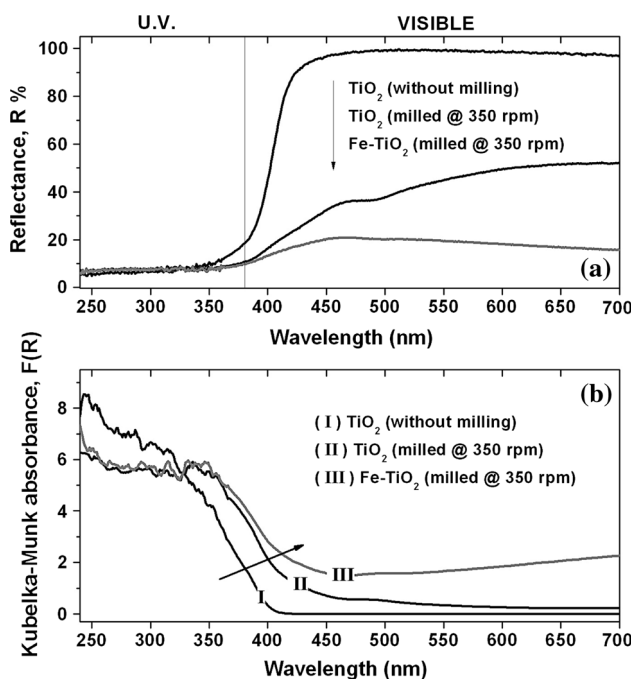
Fig. 6 Plot of Kubelka–Munk transform versus the energy of the light absorbed for (I) undoped TiO₂ (without milling), (II) undoped TiO₂ (milled @ 350 rpm), and (III) Fe-doped TiO₂ powder milled at a rotation speed of 350 rpm

similar to usual UV–Vis spectroscopy where reflected light, instead of transmitted light, is collected. Analogous to transmittance for liquids, reflectance, $R$, is a useful parameter to quantify the amount of light reflected by a solid surface. A correspondent measurement for light absorption can be defined through a parameter called the Kubelka–Munk function, $F(R)$ [31], analogous to absorbance for liquids

$$F(R) = \frac{(1-R)^2}{2R} = \frac{\alpha}{S},\tag{8}$$

where $\alpha$ and $S$ are the absorption and scattering coefficients, respectively. Equation (8), also known as being the Kubelka–Munk absorbance for solids, corresponds to the Beer–Lambert law for liquids.

The absorption coefficient, $\alpha$, is related to the incident photon energy ($E = (1239.7/\lambda)$ [32] ) by means of the Tauc's equation [21]:

$$\alpha = \frac{A(E - E_g)^m}{E},\tag{9}$$

where $A$ is a constant that depends on the properties of the material, $E_g$ is the band-gap energy, and $m$ is a constant that can take different values depending on the type of electron transition: for a direct allowed transition $m = \frac{1}{2}$ and for an indirect allowed transition $m = 2$ [21]. Therefore,

$$F(R) = \left(\frac{\alpha}{S}\right) = \frac{1}{S} \frac{A(E - E_g)^m}{E}.\tag{10}$$

For a direct allowed transition, the previous equation can be written as follows:

$$[F(R)E]^{1/2} = B(E - E_g).\tag{11}$$

In Eq. (11) $B = (A/S)^{1/2}$ is a constant and $[F(R)\,E]^{1/2}$ is the Kubelka–Munk transform. Figure 6a shows the UV–Vis diffuse reflectance spectra of undoped TiO₂ samples compared with Fe-doped TiO₂. The raw data generating the reflectance spectra were transformed to Kubelka–Munk function values (the so-called Kubelka–Munk absorbance) according to Eq. (8), and the results are plotted in Fig. 6b.

The experimental results indicated that the undoped and un-milled TiO₂ powder shows strong photoabsorption only at wavelengths shorter than 400 nm (i.e., in the UV range), which occur due to the charge transfer (CT) from the valence band (mainly formed by $2p$ orbitals of the oxide anions) to the conduction band (mainly formed by $3d$ $t_{2g}$ orbitals of the Ti$^{4+}$ cations) [33]. On the other hand, considering the undoped TiO₂ sample, that is, the one that has been milled at a rotation speed of 350 rpm, it was found that the absorption edge was shifted to longer wavelengths (i.e., red shift). Indeed, this is a very interesting result because it clearly shows that the milling process has promoted changes over the material's optical properties. The most probable explanation could be related to the milling process that causes the formation of particles with irregular shapes, the appearance of defects in the TiO₂ lattice and changes in its crystalline size, which is in agreement with the XRD results.

In the meantime, it was found that the Fe-doped TiO₂ sample (also milled at a rotation speed of 350 rpm) had an even more pronounced red shift than the undoped one (subjected to the same milling conditions). This incremental in the absorption edge shift to a longer wavelength is due to the presence of the iron dopant, which can decrease the energy band-gap ($E_g$) of TiO₂, and thus extending the utilization of the visible light. In order to calculate the $E_g$ energies of the TiO₂ samples, the Kubelka–Munk function values were reprocessed to obtain the Kubelka–Munk transform, $[F(R)E]^{1/2}$ (see Eq. (8)), which has been plotted against incident photon energy, $E$, as shown in Fig. 7. For practical purposes, the energy band-gap value was calculated by drawing a line that is tangent to the point of inflection on the curve, and the value of $E = (1239.7/\lambda$, eV) in the point of intersection of the tangent line with the horizontal axis, corresponds to the $E_g$ value. It is important to refer that the point of inflection is found by taking the first derivative of the curve; that is, the point at which the value of the first derivative coefficient begins to decrease after increasing is the point of inflection.

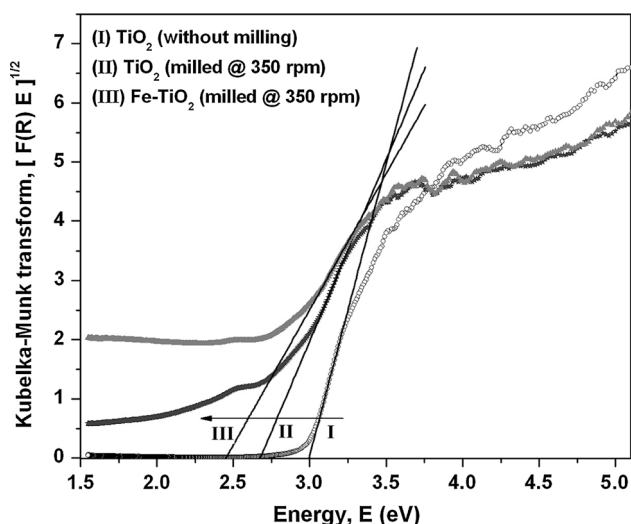It can be observed that the $E_g$ value (3.0 eV) for the bare TiO₂ catalyst (undoped and non-milled) is clearly higher

Fig. 7 Plot of Kubelka–Munk transform versus the energy of the light absorbed for undoped TiO$_2$ (without milling and milled @ 350 rpm) and Fe-doped TiO$_2$ powder milled at a rotation speed of 350 rpm



Fig. 8 (M–H) curves of Fe-doped TiO$_2$ powders. **a** Fe–TiO$_2$ milled @ 250, 300, and 350 rpm. **b** Undoped TiO$_2$ and undoped TiO$_2$ milled @ 350 rpm

compared to the band-gap values of the milled/undoped TiO$_2$ catalysts ($\sim$2.68 eV). Moreover, these results also show that for the same milling rotation speed (350 rpm), the band-gap energy of the Fe-doped TiO$_2$ powders is even lower ($E_g = 2.45$ eV) than the milled/undoped TiO$_2$ catalyst, which is in good agreement with previous reports [34]. The decrease in energy band-gap and the associated absorption enhancement in the visible region can be ascribed to the formation of a dopant energy level (Fe$^{4+}$/Fe$^{3+}$) within the band-gap of TiO$_2$ (nearer the valance band), which results in the excitation of Fe$^{3+}$ 3$d$-electrons from the dopant energy level to the TiO$_2$ conduction band (CT transition) [35].

Magnetic properties of Fe-doped TiO$_2$ powders

Magnetization ($M$) versus magnetic field ($H$) curves of bare and Fe-doped TiO$_2$ powders (taken from 100 mg of powder) are displayed in Fig. 8. A maximum saturating field of 20 kOe was applied and, then decreased down to −20 kOe by step of 2 kOe, and back up to 20 kOe. The field steps were decreased down to 200 Oe around the zero field range for better resolution.

The ferromagnetic hysteresis (M–H) curves are clearly found for all samples, which indicate that the Fe-doped and undoped TiO$_2$ powders (see Fig. 8a, b, respectively) exhibit ferromagnetic behavior, although for undoped TiO$_2$ powders this phenomenon is almost insignificant when compared with the Fe-doped TiO$_2$ samples.

From Fig. 8a, it can be pointed out that the saturation magnetization ($M_S$) and the coercivity values of Fe-doped
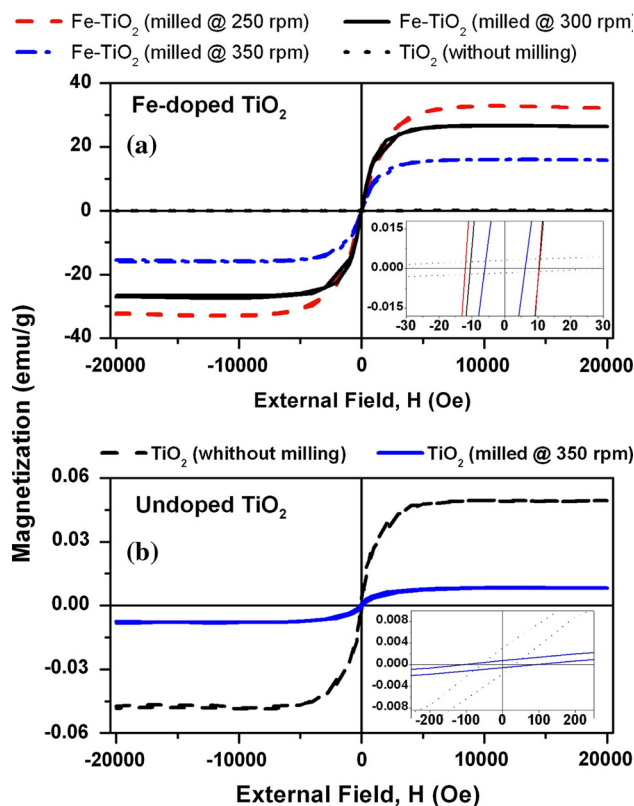
TiO$_2$ powders milled at 250 rpm are about 32.5 emu/g and 14 Oe, respectively. Moreover, it can be observed that the coercivity and $M_S$ values of Fe-doped TiO$_2$ samples decrease with increasing milling rotation speed, as they are about 16 emu/g and 7 Oe, respectively, for samples milled at 350 rpm. It is well known that the saturation magnetization values of Fe metal and iron oxides are, respectively, about 220 and 130 emu/g [36], which are much larger than the $M_S$ values obtained herein, because for the milled Fe-doped TiO$_2$ powders, they are ranging from about 16 to 32.5 emu/g. This magnetic behavior indicates that the ferromagnetism of milled Fe-doped TiO$_2$ powder does not result from the presence of minor residual metallic Fe and iron oxides particles/clusters in the milled powder, but from Fe-doped TiO$_2$ powder matrices.

Some research works suggest that structural defects can induce magnetic changes [37] because they contribute to promote the ART. According to our XRD patterns it is possible to observe that the increase on the ball-milling rotation speed promotes the ART, because the ball's mechanical action favors powder's deformation and induces the formation of more defects during the rising of milling speed.

According to Coey et al. [36], a possible origin of room-temperature ferromagnetism of Fe-doped $TiO_2$ semiconductor is an F-center-bound magnetic polaron, which is formed by an electron trapped in an oxygen vacancy and its neighboring magnetic impurity ions. The oxygen vacancies are introduced to keep the crystal charge neutrality after $Ti^{4+}$ is replaced by $Fe^{3+}$ ions [36]. According to Fig. 7a, it is possible to perceive that the $M_S$ values for Fe-doped samples decrease with increasing milling rotation speed. A possible explanation may be related with the anatase–rutile phase junctions (ARJs) between the anatase and rutile phases, which arise during the evolution of ART (enhanced by the increase in ball-milling rotation speed). The developing of ARJs can reduce the number of the trapped electrons and may destroy the magnetic polarons in Fe-doped $TiO_2$ milled samples, which in turn results on the decrease in magnetization. However, the true magnetic mechanism of the mixed anatase/rutile Fe-doped $TiO_2$ semiconductor is very complex and thus, it remains as an open issue that needs further detailed studies.

Photocatalytic activity

The photocatalytic activity of undoped and Fe-doped $TiO_2$ photocatalysts milled at different rotation speeds was evaluated in terms of degradation of Rh-B under UV light irradiation.

Figure 9 shows, for different irradiation times, the absorption spectra of Rh-B (5 mg/L) in the presence of a pressed disk sample obtained from undoped $TiO_2$ nanoparticles milled at a rotation speed of 300 rpm.

As can be observed, the maximum absorption peak, at around 564 nm, gradually decreases during UV irradiation. For this sample, the initial absorbance decreased about 32 % after 120 min. In fact, the color of the dye changed from dark-red to light red, hence indicating that the chemical oxidation–reduction mechanisms are occurring at the surface of the photocatalyst. It is important to refer that under similar UV irradiation conditions, the absence of the photocatalyst did not affect the Rh-B absorption curves.

Using the absorption spectra of all the produced samples, it was possible to calculate the corresponding photocatalytic efficiencies ($\eta$) by applying Eq. (5). Figure 10 shows the variation with time of the photocatalytic degradation of Rh-B aqueous solution in the presence of pressed disk samples, produced from undoped and Fe-doped $TiO_2$ nanoparticles and processed at different milling speeds.

By using the UV–Vis spectroscopy data from all the produced samples, it was possible to determine the photodegradation rate constant, $k$, of Rh-B dye. Assuming pseudo-first-order reaction kinetics and taking the corresponding natural logarithm, a plot of ln ($C_t/C_0$) as a function of UV irradiation time can be drawn, which has a linear-like response. In this way, the photodegradation rate constants can be obtained from the slopes of the fitting lines. The calculated $k$ values are recorded in Table 5.

Regarding the undoped $TiO_2$ samples, it is possible to observe that the effect caused by the increase of milling
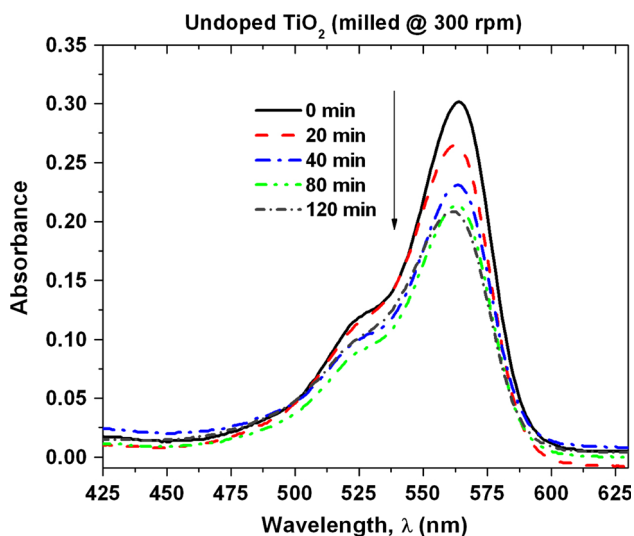


Fig. 9 Absorption spectra of Rh-B aqueous solution acquired at different irradiation times. The absorption data refer to the photocatalytic action of an undoped $TiO_2$-based pressed disk sample (obtained from $TiO_2$ nanoparticles milled at a rotation speed of 300 rpm) inserted in a flask filled with about 100 mL of Rh-B aqueous solution
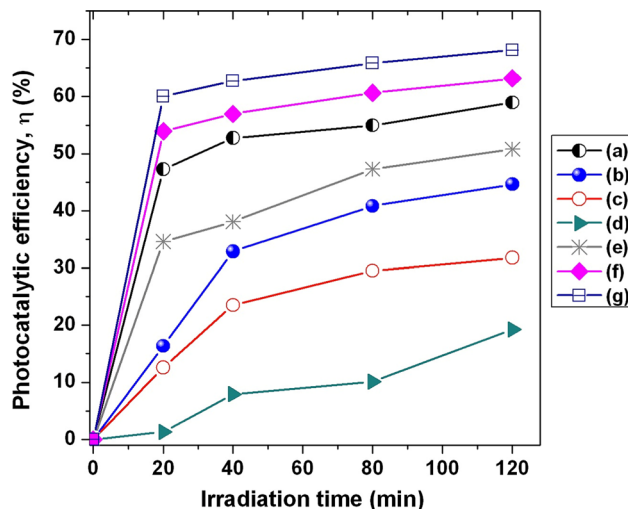


Fig. 10 Photocatalytic degradation, over time, of Rh-B aqueous solution in the presence of $TiO_2$-based pressed disk samples containing: a undoped $TiO_2$/without milling, b undoped $TiO_2$ milled @ 250 rpm/, c undoped $TiO_2$/milled @ 300 rpm, d undoped $TiO_2$/milled @ 350 rpm, e Fe-doped $TiO_2$/milled @ 250 rpm, f Fe-doped $TiO_2$/milled @ 300 rpm, and g Fe-doped $TiO_2$/milled @ 350 rpm

**Table 5** Parameters of photocatalytic degradation for Rh-B in undoped and Fe-doped TiO$_2$ powders processed by milling process

| Rotation speed (rpm) | Undoped TiO$_2$ | | Fe-doped TiO$_2$ (10 wt% Fe) | |
|---|---|---|---|---|
| | Photocatalytic efficiency, $\eta$ (%) | Rate constant, $k$ (min$^{-1}$) | Photocatalytic efficiency, $\eta$ (%) | Rate constant, $k$ (min$^{-1}$) |
| 0 | 58.97 | $5.76 \times 10^{-3}$ | – | – |
| 250 | 44.65 | $4.79 \times 10^{-3}$ | 50.75 | $5.04 \times 10^{-3}$ |
| 300 | 31.79 | $3.05 \times 10^{-3}$ | 63.18 | $6.37 \times 10^{-3}$ |
| 350 | 19.26 | $1.74 \times 10^{-3}$ | 68.14 | $7.19 \times 10^{-3}$ |

speed is detrimental to the photocatalytic efficiency. We believe that the main explanation for this behavior is probably due to the ART transformation caused by the milling process. Actually, it is well known that anatase TiO$_2$ is a better photocatalyst than rutile TiO$_2$ [38]. From our XRD patterns it was possible to determine the variation in fraction of anatase phase, $X_A$ (%) with the milling rotation speed. The results presented in Table 2 show that content of rutile phase increased from $\sim$17.6 to 33.7 % as the milling speed ranged from 0 to 350 rpm.

In what concerns the Fe-doped TiO$_2$ samples, it is possible to verify that, in general, they exhibit the highest photocatalytic efficiencies (higher than 60 % at around 120 min) for Rh-B degradation under UV irradiation. In addition, the Fe-doped TiO$_2$ samples prepared at higher milling speeds show better photocatalytic efficiency, despite having higher content of rutile phase. Moreover, it can be pointed out that the Fe-doped TiO$_2$ milled at a rotation speed of 350 rpm has better photocatalytic efficiency than all the other produced samples. Therefore, it is possible to conclude that in a general way, the incorporation of iron, via the milling process, has enhanced the photocatalytic efficiency of TiO$_2$ nanoparticles. The favorable effect of Fe-ion dopant in the enhancement of photocatalytic activity can be explained by the extended lifetimes of electron/holes pairs due to the double Fe$^{3+}$ function, because it can act as an electron and hole scavenger. Niu et al. [39] considered that there exist two configuration energy levels (see Fig. 11), that is, the oxidation level (Fe$^{3+}$/Fe$^{4+}$) falling above the valence band edge of undoped TiO$_2$ and the reduction level (Fe$^{3+}$/Fe$^{2+}$), which is under the conduction energy level of undoped TiO$_2$.

According to Niu et al. [39], the first step consists on the formation of Fe$^{2+}$ ions that results by the transfer of photogenerated electrons from TiO$_2$ to Fe$^{3+}$ (Eq. (12)). Fe$^{2+}$ ion is relatively unstable when compared to Fe$^{3+}$ ion, which have half-filled $3d^5$ orbital [39]. Hence, the trapped charges can be released from Fe$^{2+}$ ions and afterward migrate to the semiconductor surface to initiate the photocatalytic reactions. In this sense, Fe$^{2+}$ ions can be oxidized to Fe$^{3+}$ ions by transferring electrons to molecular oxygen (absorbed on the surface of TiO$_2$) to form superoxide anions, which are highly reactive oxygen species
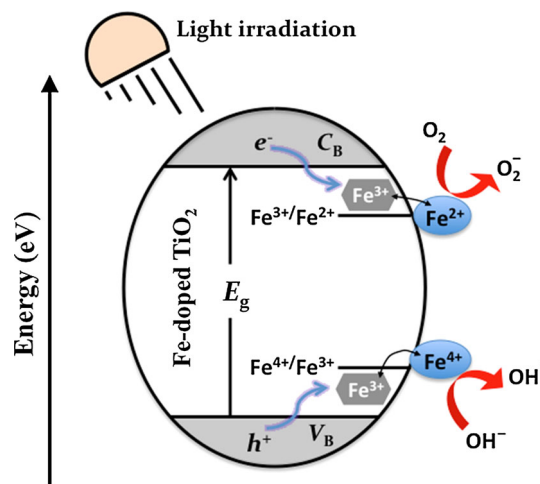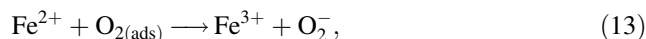


**Fig. 11** Schematic diagram showing the mechanism of CT from excited TiO$_2$ to the different energy levels of Fe$^{3+}$ ions; $C_B$ and $V_B$ are the energy levels of the conduction and valence bands of the semiconductor, respectively [40]

(Eq. (13)). In the mean time, Fe$^{3+}$ ions can also act as holes trap (Eq. (14)), because the energy level for Fe$^{4+}$/Fe$^{3+}$ is above the valence band energy of undoped TiO$_2$. Therefore, Fe$^{4+}$ ions can be reduced to Fe$^{3+}$ ions by capturing electrons, whilst surface hydroxyl groups transforms into hydroxyl radicals (Eq. (15)).

$$Fe^{3+} + e^- \longrightarrow Fe^{2+}, \qquad (12)$$

$$Fe^{2+} + O_{2(ads)} \longrightarrow Fe^{3+} + O_2^-, \qquad (13)$$

$$Fe^{3+} + h^+ \longrightarrow Fe^{4+}, \qquad (14)$$

$$Fe^{4+} + OH^- \longrightarrow Fe^{3+} + OH^. \qquad (15)$$

We believe that the electron and hole scavenger ability of Fe$^{3+}$ ions is the main feature that helps to explain the higher photocatalytic activity observed for our Fe-doped TiO$_2$ samples, despite the occurrence of the ART transformation promoted by the milling process. Moreover, we also believe that the crystal sizes of the ball-milled Fe-doped TiO$_2$ samples must play a significant role in determining the beneficial effect of using higher milling speeds to enhance the photocatalytic activity of Fe-doped samples.

From Table 3, we found that Fe-doped $TiO_2$ samples, which were milled at higher rotation speeds, resulted in rutile crystallites with lower sizes. As the crystallite size is decreased, the particle's surface-to-volume ratio is increased; then the photo-generated electron/hole pairs could undergo a short pathway to migrate to the surface and the $e^-/h^+$ volume recombination rate should decrease giving rise to the improvement of photocatalytic activity.

## Conclusions

This research work evaluated the benefits of using ball-milling process as a powerful, low-cost, and "green" method to produce Fe-doped $TiO_2$ nanoparticles, which can be applied as an efficient photocatalyst for large-scale photocatalytic oxidation of dye pollutants present in the effluents of textile industries. Based on the results of the experimental activity, the following conclusions may be drawn:

- The ball-milling rotation speed strongly influences the $TiO_2$ phase composition since it was verified that for higher milling it occurs a more pronounced ART transformation. Moreover, it was verified that the ball-milling process also induces changes in the $TiO_2$ nanoparticles crystalline lattice parameters. On the other hand, the angular position of some XRD peaks was slightly shifted after Fe-doping, thus indicating some distortions of $TiO_2$ crystal lattice promoted by the iron dopant.
- For the non-milled $TiO_2$, the IEP was found to be $\sim$ pH 5.2. However, after being subjected to different ball-milling rotation speeds, the sample experienced some variations in its IEP. This behavior is related with the milling-induced phase transformation, that is, for higher rotation speeds, more anatase transforms into rutile phase.
- The SEM analysis shows that the $TiO_2$ nanoparticles are irregular in shape, randomly organized and tend to form agglomerates and its surface morphology did not significantly changed after ball milling or iron doping. Nonetheless, the milled $TiO_2$ nanoparticles appear to be rougher which may enhance the absorption of the dyes due to its higher surface area.
- The band-gap energy for the un-milled/pure $TiO_2$ nanoparticles is higher in comparison with the obtained values for the milled/pure $TiO_2$ ones, decreasing with the increase of the rotation speed. Moreover, the band-gap energy for the Fe-$TiO_2$ nanoparticles is still lower than the milled/pure $TiO_2$ samples.
- The Fe-doped $TiO_2$ powders exhibit a ferromagnetic behavior and the saturation magnetization ($M_s$) values decrease with the increase of the ball-milling rotation speed.

- For the undoped $TiO_2$ nanoparticles, the effect caused by the increase in the milling speed is detrimental to the photocatalytic efficiency that may be explained due to the ART transformation. The Fe-doped $TiO_2$ powders exhibit the highest photocatalytic efficiencies (higher than 60 % at around 120 min) for Rh-B degradation under UV light irradiation. In addition, the Fe-doped $TiO_2$ samples milled at higher rotation speeds presented better photocatalytic efficiency despite having higher content of rutile phase.
- As a general conclusion, the incorporation of iron, via ball-milling process, in $TiO_2$ nanoparticles has enhanced their photocatalytic activity.

## References

1. Wang S, Zhu Z (2007) Effects of acidic treatment of activated carbons on dye adsorption. Dyes Pigm 75:306–314. doi:10.1016/j.dyepig.2006.06.005
2. Hoffmann MR, Martin ST, Choi W et al (1995) Environmental applications of semiconductor photocatalysis. Chem Rev 95:69–96. doi:10.1021/cr00033a004
3. Fujishima A, Rao TN, Tryk DA (2000) Titanium dioxide photocatalysis. J Photochem Photobiol C 1:1–21
4. Tong T, Zhang J, Tian B et al (2008) Preparation of $Fe^{3+}$-doped $TiO_2$ catalysts by controlled hydrolysis of titanium alkoxide and study on their photocatalytic activity for methyl orange degradation. J Hazard Mater 155:572–579. doi:10.1016/j.jhazmat.2007.11.106
5. Kim DH, Jang JS, Goo NH et al (2009) Structural characterization and effect of dehydration on the Ni-doped titanate nanotubes. Catal Today 146:230–233. doi:10.1016/j.cattod.2009.04.007
6. Zhu J, Zheng W, He B et al (2004) Characterization of Fe–$TiO_2$ photocatalysts synthesized by hydrothermal method and their photocatalytic reactivity for photodegradation of XRG dye diluted in water. J Mol Catal A 216:35–43. doi:10.1016/j.molcata.2004.01.008
7. Yuan X-L, Zhang J-L, Anpo M, He D-N (2010) Synthesis of $Fe^{3+}$ doped ordered mesoporous $TiO_2$ with enhanced visible light photocatalytic activity and highly crystallized anatase wall. Res Chem Intermed 36:83–93. doi:10.1007/s11164-010-0117-6
8. Haruta M (1997) Novel catalysis of gold deposited on metal oxides. Catal Surv Jpn 1:61–73
9. Kitano M, Takeuchi M, Matsuoka M et al (2007) Photocatalytic water splitting using Pt-loaded visible light-responsive $TiO_2$ thin film photocatalysts. Catal Today 120:133–138. doi:10.1016/j.cattod.2006.07.043
10. Chatterjee D, Mahata A (2001) Photoassisted detoxification of organic pollutants on the surface modified $TiO_2$ semiconductor particulate system. Catal Commun 2:7–9
11. Zhong J, Chen F, Zhang J (2010) Carbon-deposited $TiO_2$: synthesis, characterization, and visible photocatalytic performance. J Phys Chem C 114:933–939
12. Lu X, Tian B, Chen F, Zhang J (2010) Preparation of boron-doped $TiO_2$ films by autoclaved-sol method at low temperature

and study on their photocatalytic activity. Thin Solid Films 519:111–116. doi:10.1016/j.tsf.2010.07.071

13. Chen YM, Zhong J, Chen F, Zhang JL (2010) Chinese J Catal 31:120–125

14. Serpone N, Lawless D, Disdier J, Herrmann J-M (1994) Spectroscopic, photoconductivity, and photocatalytic studies of $TiO_2$ colloids: naked and with the lattice doped with $Cr^{3+}$, $Fe^{3+}$, and $V^{5+}$ cations. Langmuir 10:643–652. doi:10.1021/la00015a010

15. Karakitsou KE, Verykios XE (1993) Effects of altervalent cation doping of titania on its performance as a photocatalyst for water cleavage. J Phys Chem 97:1184–1189. doi:10.1021/j100108a014

16. Carneiro JO, Teixeira V, Portinha A et al (2005) Study of the deposition parameters and Fe-dopant effect in the photocatalytic activity of $TiO_2$ films prepared by dc reactive magnetron sputtering. Vacuum 78:37–46. doi:10.1016/j.vacuum.2004.12.012

17. James SL, Adams CJ, Bolm C et al (2012) Mechanochemistry: opportunities for new and cleaner synthesis. Chem Soc Rev 41:413–447. doi:10.1039/c1cs15171a

18. Kaupp G (2009) Mechanochemistry: the varied applications of mechanical bond-breaking. CrystEngComm 11:388. doi:10.1039/b810822f

19. Jenkins RH, Snyder RL (1996) Introduction to X-ray powder diffractometry. Wiley-Interscience, New York

20. Spurr RA, Myers H (1957) Quantitative analysis of anatase–rutile mixtures with an X-ray diffractometer. Anal Chem 29:760–762. doi:10.1021/ac60125a006

21. Tauc J, Grigorovici R, Vancu A (1966) Optical properties and electronic structure of amorphous germanium. Phys Status Solidi 15:627–637

22. Hashimoto K, Wasada K, Toukai N et al (2000) Photocatalytic oxidation of nitrogen monoxide over titanium(IV) oxide nanocrystals large size areas. J Photochem Photobiol A Chem 136:103–109. doi:10.1016/S1010-6030(00)00329-4

23. Masterton WL, Bolocofsky D, Lee TP (1971) Ionic radii from scaled particle theory of the salt effect. J Phys Chem 75:2809–2815. doi:10.1021/j100687a017

24. Hunter RJ (1981) Zeta potential in colloid science. Academic Press, New York

25. Carneiro JO, Azevedo S, Teixeira V et al (2013) Development of photocatalytic asphalt mixtures by the deposition and volumetric incorporation of $TiO_2$ nanoparticles. Constr Build Mater 38:594–601. doi:10.1016/j.conbuildmat.2012.09.005

26. Pan X, Chen Y, Ma X, Zhu L (2003) Phase transformation of nanocrystalline anatase powders during high energy planetary ball milling. Trans Nonferrous Met Soc China 13:271–272

27. Zhou M, Yu J, Cheng B (2006) Effects of Fe-doping on the photocatalytic activity of mesoporous $TiO_2$ powders prepared by an ultrasonic method. J Hazard Mater 137:1838–1847. doi:10.1016/j.jhazmat.2006.05.028

28. Chen F, Zhao J, Hidaka H (2003) Highly selective deethylation of rhodamine B: adsorption and photooxidation pathways of the dye on the $TiO_2/SiO_2$ composite photocatalyst. Int J Photoenergy 5:209–217

29. Kormann C, Bahnemann DW, Hoffmann MR (1991) Photolysis of chloroform and other organic molecules in aqueous titanium dioxide suspensions. Environ Sci Technol 25:494–500. doi:10.1021/es00015a018

30. Jalalah M, Faisal M, Bouzid H et al (2013) Dielectric and photocatalytic properties of sulfur doped $TiO_2$ nanoparticles prepared by ball milling. Mater Res Bull 48:3351–3356. doi:10.1016/j.materresbull.2013.05.023

31. Valencia S, Marín JM, Restrepo G (2010) Study of the bandgap of synthesized titanium dioxide nanoparticles using the sol–gel method and a hydrothermal treatment. Open Mater Sci J 4:9–14

32. Kisch H, Sakthivel S, Janczarek M, Mitoraj D (2007) A low-band gap, nitrogen-modified titania visible-light photocatalyst. J Phys Chem C 111:11445–11449

33. Venkatachalam N, Palanichamy M, Murugesan V (2007) Sol–gel preparation and characterization of nanosize $TiO_2$: its photocatalytic performance. Mater Chem Phys 104:454–459. doi:10.1016/j.matchemphys.2007.04.003

34. Navio JA, Macias M, Gonzalez-Catalan M, Justo A (1992) Bulk and surface characterization of powder iron-doped titania photocatalysts. J Mater Sci 27:3036–3042. doi:10.1007/BF01154116

35. Adán C, Bahamonde A, Fernández-García M, Martínez-Arias A (2007) Structure and activity of nanosized iron-doped anatase $TiO_2$ catalysts for phenol photocatalytic degradation. Appl Catal B Environ 72:11–17. doi:10.1016/j.apcatb.2006.09.018

36. Coey JMD, Venkatesan M, Fitzgerald CB (2005) Donor impurity band exchange in dilute ferromagnetic oxides. Nat Mater 4:173–179. doi:10.1038/nmat1310

37. Tian J, Gao H, Deng H et al (2013) Structural, magnetic and optical properties of Ni-doped $TiO_2$ thin films deposited on silicon(100) substrates by sol–gel process. J Alloys Compd 581:318–323. doi:10.1016/j.jallcom.2013.07.105

38. Luttrell T, Halpegamage S, Tao J et al (2014) Why is anatase a better photocatalyst than rutile? Model studies on epitaxial $TiO_2$ films. Sci Rep 4:4043. doi:10.1038/srep04043

39. Niu Y, Xing M, Zhang J, Tian B (2013) Visible light activated sulfur and iron co-doped $TiO_2$ photocatalyst for the photocatalytic degradation of phenol. Catal Today 201:159–166. doi:10.1016/j.cattod.2012.04.035

40. Shannon RD, Pask JA (1965) Kinetics of the anatase–rutile transformation. J Am Ceram Soc 48:391–398. doi:10.1111/j.1151-2916.1965.tb14774.x